# In-Situ Electron Microscopy of Transformations of Copper Nanoparticles under Plasmonic Excitation

Francis M. Alcorn<sup>a, b</sup>, Renske M. van der Veen<sup>a, b, c,\*</sup>, and Prashant K. Jain<sup>a, b d,\*</sup>

<sup>a</sup> Department of Chemistry, University of Illinois at Urbana-Champaign, Urbana, IL 61801, USA

<sup>b</sup> Materials Research Laboratory, University of Illinois at Urbana-Champaign, Urbana, IL 61801,

USA

<sup>c</sup> Helmholtz Zentrum Berlin für Materialien und Energie GmbH, 14109 Berlin, Germany

<sup>d</sup> Beckman Institute for Advanced Science and Technology, University of Illinois at Urbana-

Champaign, Urbana, IL 61801, USA

\*Corresponding authors: Prof. Prashant K. Jain; Prof. Renske M. van der Veen

E-mail address: jain@illinois.edu; renske.vanderveen@helmholtz-berlin.de

## **Abstract**

Metal nanoparticles are attracting interest for their light-absorption properties; but such materials are known to dynamically evolve under the action of chemical and physical perturbations, resulting in changes in their structure and composition. Using a transmission electron microscope equipped for optical excitation of the specimen, the structural evolution of Cu-based nanoparticles under simultaneous electron beam irradiation and plasmonic excitation was investigated with high spatiotemporal resolution. These nanoparticles initially have a Cu core—Cu<sub>2</sub>O oxide shell structure; but over the course of imaging, they undergo hollowing *via* the nanoscale Kirkendall effect. We captured the nucleation of a void within the core which then rapidly grows along specific crystallographic directions until the core is hollowed out. Hollowing is triggered by electron-beam irradiation; plasmonic excitation enhances the kinetics of the transformation likely by the effect of photothermal heating.

**Keywords:** TEM, hollow nanostructures, nanoscale Kirkendall effect, operando measurements, diffusion, LSPR

#### Introduction

Metal nanoparticles comprised of Au, Ag, and Cu display a notable optical phenomenon known as a localized surface plasmon resonance (LSPR) arising from collective oscillations of charge carriers that makes them excellent visible light-absorbing nanoantennae. Consequently, these materials are being used in photocatalysis, single molecule spectroscopy, biomedicine, and optical devices. LSPR properties are dictated by the size, shape and chemical composition of the nanoparticles. These parameters, however, may dynamically evolve under operating conditions due to structural and chemical changes induced by plasmonic excitation. Understanding such dynamics is essential for developing robust and effective nanostructures for plasmonic devices and applications.

The dynamic evolution of nanostructures under stimulation has been studied by optical spectroscopy, <sup>18,21–25</sup> X-ray techniques, <sup>26–28</sup> and transmission electron microscopy (TEM). <sup>29–36</sup> Studies have revealed reshaping <sup>31,37–39</sup> and changes in elemental compositions <sup>26,28,30,32,40</sup> in response to perturbations such as heating and exposure to reactive species. Similar exploration of structural dynamics of metal nanostructures induced by plasmonic excitation requires a TEM equipped for probing materials under light. <sup>41</sup> Optical-excitation-coupled TEM has been used to gain insights into photocatalytic activity <sup>42–45</sup> and fast and ultrafast dynamics. <sup>46–54</sup>

Here we used a TEM equipped for optical excitation of the specimen<sup>55</sup> to probe the structural evolution of Cu-based nanoparticles, a canonical plasmonic nanostructure. <sup>20,56,57</sup> Our study uncovered that under plasmonic excitation and electron beam irradiation, Cu core—Cu<sub>2</sub>O shell nanoparticles transform to hollow Cu<sub>2</sub>O nanoshells *via* the nanoscale Kirkendall effect (NKE)<sup>21–23,32,58–66</sup> (Fig. 1). While the NKE has been studied for Cu nanoparticles by ex-situ and in-situ liquid-cell TEM,<sup>32,58–60</sup> the present study captures the dynamics of this transformation in real time with atomic resolution and reveals the impact of plasmonic excitation on this process. We capture the nucleation of voids in the Cu core; these voids then grow rapidly along specific crystallographic directions resulting in the hollow nanostructure. The hollowing process is accompanied by the formation of a two-dimensional (2D) film of Cu<sub>2</sub>O around the nanoparticle. Plasmonic excitation accelerates the kinetics of hollowing by enhancing the rate of void nucleation likely by the effect of photothermal heating.

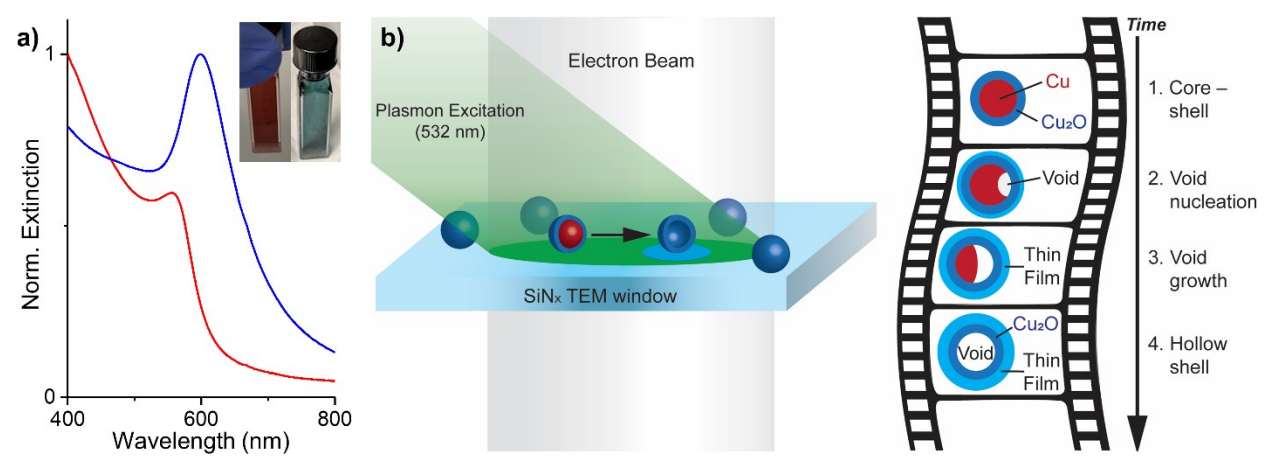


Figure 1 | Plasmonic properties of Cu nanoparticles and experimental schematic. (a) Normalized ultraviolet-visible (UV-vis) spectra of as-synthesized Cu nanoparticles (red curve) and oxidized Cu core—Cu<sub>2</sub>O shell nanoparticles (blue curve) in colloidal form. The main absorption peak of the Cu core—Cu<sub>2</sub>O shell nanoparticles arises from the LSPR of the metallic Cu core. It is red-shifted relative to the LSPR peak of the as-synthesized, unoxidized Cu nanoparticles due to the effect of the high dielectric constant of the Cu<sub>2</sub>O shell. The inset shows photographs of the (left) as-synthesized Cu nanoparticle colloid and (right) the Cu core—Cu<sub>2</sub>O shell nanoparticle colloid in cuvettes. (b) Experimental schematic. Cu core—Cu<sub>2</sub>O shell nanoparticles on silicon nitride (SiN<sub>x</sub>) substrates were studied at the single-nanoparticle level by TEM under plasmonic excitation (532 nm laser) and electron-beam irradiation. (Right) Schematic of the dynamic evolution of Cu—Cu<sub>2</sub>O nanoparticles. In the course of imaging, a void appears within the nanoparticle at the metal—metal-oxide interface, which grows to produce a hollow oxide nanoshell. Concomitantly, a thin film of copper oxide forms on the substrate around the nanoparticle, as depicted by the light-blue disk.

#### Results and discussion

Copper nanoparticles were synthesized using a wet synthetic method with oleic acid and trioctylamine ligands (see section on "Cu nanoparticle synthesis" in the Supporting Information). As a plasmonic material, unoxidized  $Cu^0$  nanoparticles exhibit a prominent light absorption band centered around ~560 nm (red curve in Fig. 1a and Fig. S1), which is attributable to their localized surface plasmon resonance (LSPR). Given the propensity of copper to oxidize, air exposure at ambient temperatures results in formation of a shell of cuprous oxide  $(Cu_2O)$ , producing a core—shell nanostructure. The growth of a high dielectric constant medium, i.e.,  $Cu_2O$ , around the Cu core causes a red shift of the LSPR peak to ~600 nm (blue curve in Fig. 1a and Fig. S1); but the LSPR of the metallic Cu core remains the primary mode of light absorption. Cu

These Cu–Cu<sub>2</sub>O core–shell nanoparticles were loaded onto silicon nitride (SiN<sub>x</sub>) substrates, and, using the DETEM, they were imaged under constant plasmonic excitation accomplished by irradiation with a 532 nm pulsed nanosecond laser (Figs. 1b and S2) with a <1 ns pulse duration and operating at an 80 kHz repetition rate. The laser was incident on the sample in an elliptical spot with dimensions of ~50 and ~20  $\mu$ m along the two axes corresponding to a spot area of ~700  $\mu$ m<sup>2</sup>. Laser power was maintained below 25 mW corresponding to a maximum

intensity of 3500 W/cm² and a maximum fluence of 50 mJ/cm² per pulse. In the course of imaging, nanoparticles subjected to plasmonic excitation convert from a core—shell nanostructure to a hollow spherical nanoshell morphology (Fig. 1b, right), as shown by snapshots (Fig. 2) from a movie of a selected single nanoparticle (Supporting Movie 1). At early times (Fig. 2a), the nanoparticle has a Cu² core (region of darker contrast) and a Cu²O shell (region of lighter contrast). Around 663 s, a void (shown by green arrow in Fig. 2b) appears within the Cu² core, which grows across the nanoparticle to produce the eventual hollow nanoshell (Fig. 2f). The full movie is included in the Supporting Information (Supporting Movie 1). In addition, snapshots from additional movies showing hollowing of randomly selected nanoparticles under plasmonic excitation are provided in Fig. S3.

Concurrent with the disappearance of the Cu core, there is the appearance of a film of material around the nanoparticle (Fig. S4a&b), which continuously grows outward as the core shrinks. Elemental mapping by energy-filtered TEM (EFTEM) (Fig. S4d) shows the presence of O (Fig. S4e) and Cu (Fig. S4f) indicating that the film is comprised of copper oxide. The material has crystalline domains with lattice fringes consistent with {111} planes of Cu<sub>2</sub>O (Fig. S4c). Cu<sub>2</sub>O is thus the likely composition. The contrast of this material is much lighter than the contrast of the Cu<sub>2</sub>O shell of the initial nanostructure and nearly similar to the background, which suggests that Cu<sub>2</sub>O is formed as a 2D thin film on the substrate around the nanoparticle, unlike the threedimensional growth of the Cu<sub>2</sub>O shell seen in other studies.<sup>22</sup> Thus, it appears that Cu atoms diffuse out of the core, migrate through the shell, and deposit onto the substrate as a thin film of copper oxide. The formation of stable copper oxide is the thermodynamic driving force for the oxidation and hollowing of the Cu core; kinetically, it is triggered by the action of the electron beam and/or plasmonic excitation (vide infra). Under the low-pressure (~10<sup>-5</sup> Pa) conditions of the TEM, the source of oxygen in this reaction is likely oxygen adsorbed on the substrate. Treatment of the substrate with an Ar + O<sub>2</sub> plasma increased the rate of Cu oxidation (see Supporting Information section on "Thin film growing around nanoparticles"). This observation coupled with the thin-film morphology of the copper oxide indicates that Cu emanating from the nanoparticle reacted with oxygen adsorbed on the substrate. The film formed on the substrate appears to grow isotropically around the nanoparticle. This indicates that the formation of the 2D Cu<sub>2</sub>O film is limited by the availability of surface-adsorbed oxygen for the reaction with Cu; the isotropic morphology of the film therefore reflects the profile of adsorbed oxygen around the nanoparticle.

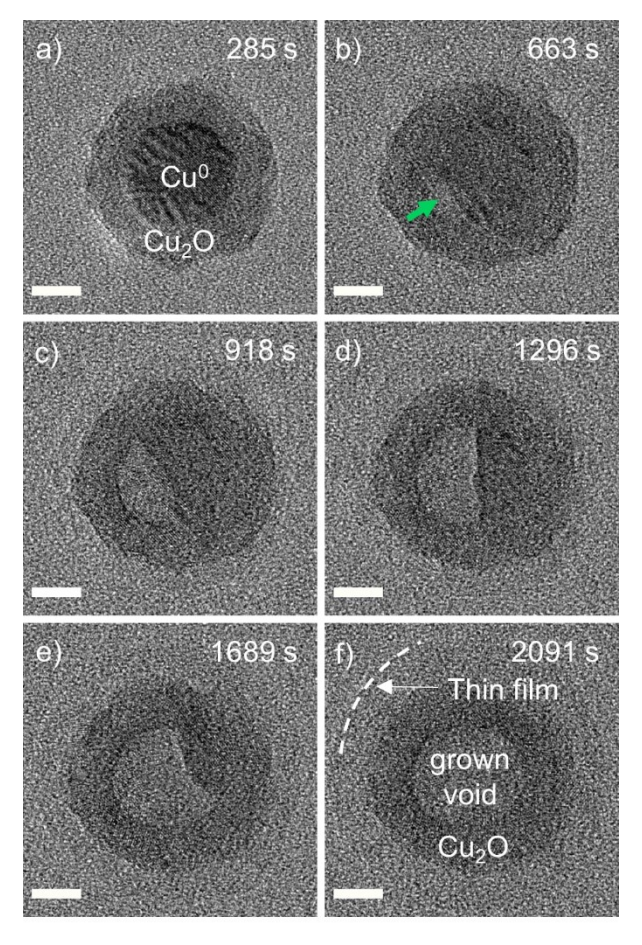


Figure 2 | Snapshots from an in-situ movie acquired under plasmonic excitation showing void formation and hollowing. At early stages (a), the nanoparticle has a core–shell structure with a Cu<sup>0</sup> core (region of darker contrast) and a Cu<sub>2</sub>O shell (region of lighter contrast). Around the 633 s time point (b), a void appears at one edge of the core, as indicated by the green arrow. This void grows across the core (c–e) until a net hollow nanoshell is produced (f). Concomitantly with the hollowing, a thin film is formed around the nanoparticle. This film consists of copper oxide that likely forms by the reaction of Cu with oxygen adsorbed on the substrate. Scale bars represent a length of 5 nm.

The hollowing is a morphological outcome of the manner in which Cu is oxidized and is in fact an example of the NKE, a nanoscale analog of the Kirkendall effect. 61–66 To elaborate, oxidation occurs via the outward migration of Cu from the core along with inward migration of O toward the core. However, Cu atoms diffuse through the Cu<sub>2</sub>O shell faster than O atoms. This asymmetry in diffusion rates results in a net outward flow of Cu resulting in the accumulation of vacancies in the core. If the core gets supersaturated with vacancies, the latter condense into a void nucleus to minimize interfacial energy. A void nucleus that is larger than a critical size can spontaneously grow by coalescence with newly formed vacancies. In this manner, the void grows across the core, resulting in a hollow nanoshell. Hollowing of the Cu–Cu<sub>2</sub>O nanoparticles did not take place without constant electron-beam irradiation. Electron irradiation appears to be necessary

to trigger the reaction of Cu with oxygen inducing the NKE and hollowing. Electron beam-induced hollowing has been observed in the past and putatively attributed to core melting, etching, ablation, and evaporation. These processes do not likely contribute in the present study as the Cu core remains crystalline throughout the hollowing process; furthermore, the concomitant hollowing and oxide thin film growth support the NKE mechanism. Oxidation of Cu is spontaneous in the absence of electron irradiation but the NKE is kinetically prohibited by the low diffusivity for transport of Cu through the Cu<sub>2</sub>O shell. In such a case, the electron irradiation serves to enhance the rate of diffusion by beam-induced heating of the nanoparticles and/or radiation-enhanced diffusion. In the latter process, electron bombardment generates defects within the Cu<sub>2</sub>O shell, which results in enhanced diffusivity of Cu through the shell.

Leveraging the spatiotemporal resolution of TEM, the hollowing process was investigated further to reveal the nanoscale aspects underlying this chemical transformation. Eighty-nine movies of individual core–shell nanoparticles undergoing hollowing under plasmonic excitation were analyzed; the key features observed in each case are summarized in Table S1. Most commonly, hollowing was initiated with the nucleation of a single void. 22,65 This was the case in 65 instances. Often the void nucleated at the metal–metal-oxide interface. The high defect density and surface energy associated with the interface favor the nucleation of the voids there.

In four instances, two voids nucleated in a single core—shell nanoparticle (Fig. 3a). However, no common distinguishing structural features were identified across these four nanoparticles. Rather the nucleation of a void appears to be a stochastic event, for which two-void nucleation is less probable than single-void nucleation and three-void nucleation is less probable than two-void nucleation. This expected trend is in line with the observations (Fig. 3b). Finally, 20 nanoparticles did not undergo hollowing at all—no void nucleation occurred—within the time span of the experiment.

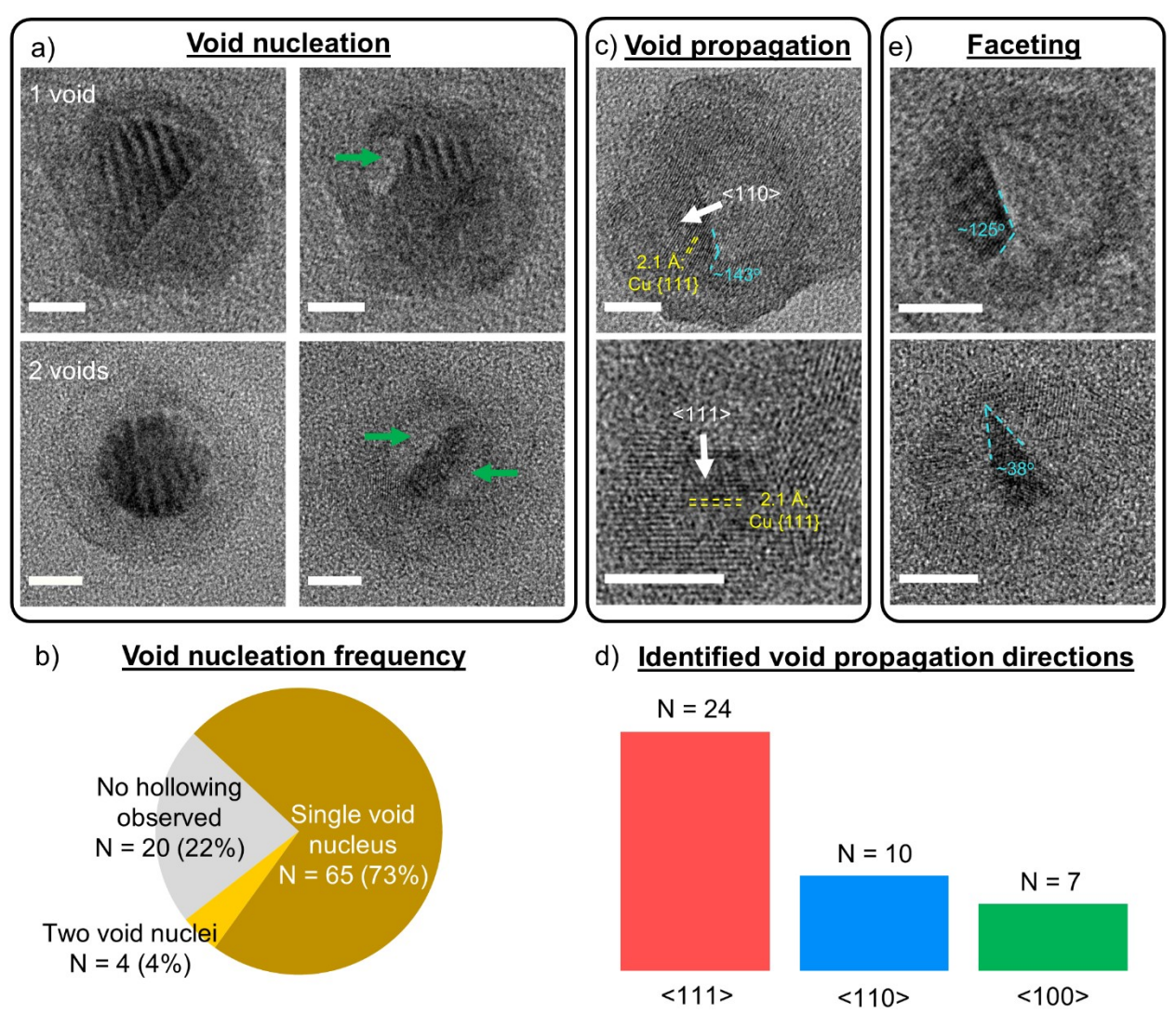


Figure 3 | Spatiotemporal aspects of the hollowing process under plasmonic excitation. Notable trends in the hollowing of a Cu core–Cu<sub>2</sub>O shell nanoparticle: (a) Snapshots before (left) and after (right) void nucleation showing an example of single-void nucleation (top) and two-void nucleation (bottom). Voids are marked by green arrows. (b) Pie chart showing the number and % of instances of zero-void (no hollowing), single-void, and two-void nucleation in a set of 89 nanoparticles. (c) Direction of void growth (shown by the white arrow and labeled crystallographic axis), and (d) number of instances of the void growing along  $\langle 111 \rangle$ ,  $\langle 110 \rangle$ , and  $\langle 100 \rangle$  directions. Note that multiple growth directions could be identified for a single nanoparticle as void growth is not generally unidirectional. (e) Faceting of the walls of the growing void, where the observed angle of ~125° is consistent with the intersection of (111) and (100) planes, and that of ~35° is consistent with the intersection of (111) and (110) planes. Image scale bars are 5 nm in length.

We also examined the spatiotemporal nature of void growth by leveraging the atomic resolution of probing. In the course of hollowing, a void propagates along multiple crystallographic directions. We identified these directions in several movies where lattice fringes were prominent within the shrinking core (Fig. 3c). From the angle between the instantaneous propagation direction (perpendicular to the void front) and the known lattice planes of the face-centered cubic (FCC) crystal structure of Cu, we identified instances of propagation along (100), (110), and (111)

directions (Fig. 3d). Our analysis was restricted to these directions due to the limited precision with which these angles could be measured.  $\langle 111 \rangle$  was the most common propagation direction, which is attributable to  $\{111\}$  facets having the lowest surface energy among  $\{111\}$ ,  $\{110\}$ , and  $\{100\}$  facets. <sup>78</sup> In 38 movies, the propagation direction was not assignable to the  $\langle 100 \rangle$ ,  $\langle 110 \rangle$ , or  $\langle 111 \rangle$  directions: there was insufficient resolution to determine lattice fringes or the angles between known planes and the void front did not agree with expected angles.

We observed that the walls of the growing void were faceted (Fig. 3e). Across  $\sim 30\%$  of the nanoparticles, the boundaries between the void and the remaining Cu<sup>0</sup> core showed sharp facets. Angles between these facets match the angles between the crystallographic planes of an FCC lattice. Fig. 3e shows two examples. In the first example, late in the hollowing process, a sharp corner with an included angle of  $\sim 125^{\circ}$  develops in the remaining Cu<sup>0</sup>, consistent with the intersection of (111) and ( $\overline{1}$ 00) planes:

$$\theta = \cos^{-1}([111] \cdot [\overline{1}00]) = \cos^{-1}\left(-\frac{1}{\sqrt{3}}\right) = 125^{\circ}$$
.

In the second example, hollowing started from two void nuclei. Immediately prior to the meeting of the voids, a sharp corner with an included angle of  $\sim 38^{\circ}$  develops in the remaining Cu<sup>0</sup>. This angle is consistent with the intersection of (111) and (110) planes:

$$\theta = \cos^{-1}([111] \cdot [110]) = \cos^{-1}\left(\frac{2}{\sqrt{6}}\right) = 35^{\circ}$$
.

To understand the role of plasmonic excitation in the hollowing process, we conducted several control experiments. Nanoparticles irradiated with the laser without constant electron-beam irradiation showed no signs of hollowing even after 3 h (Fig. S5). Conversely, under electron-beam irradiation without laser irradiation, nanoparticles were observed to hollow. Thus, plasmon excitation does not drive hollowing; rather it has a catalytic effect, as evidenced by an additional study that compares the hollowing of nanoparticles with and without plasmon excitation under equivalent electron-beam irradiation (see section "Estimated electron dose rates" in the Supporting Information). Voids were found to nucleate faster under plasmon excitation than in the absence of it (Fig. 4). The waiting time to nucleate a void was shorter for 4 of 5 nanoparticles that hollowed under plasmonic excitation than for nanoparticles that hollowed without plasmonic excitation (Fig. 4b&c). The fifth nanoparticle behaved in a different manner and was excluded as

an outlier (Fig. S6). Although the small sample size (N = 5) reduces confidence, statistical testing of these two populations by a Welch's unpaired two-tailed test indicate a statistically significant effect (p < 0.05) thereby implying that plasmonic excitation enhances the probability of void nucleation. Since void nucleation is the limiting event for hollowing,  $p^{24,25}$  this results in an overall enhanced rate of hollowing under plasmonic excitation. The rate of void propagation (defined as the change in the void area divided by the total time required for hollowing (Tables 1 and S2)) also increases under plasmonic excitation; however, the effect may not be statistically significant as determined by a t-test (p > 0.05). Higher throughput experimentation, a common limitation of single-nanoparticle-level in-situ TEM studies, would enable higher confidence in the observed kinetic trends attributed to plasmonic excitation.

Table 1 | Kinetics of Hollowing, i.e., Waiting Time for Void Nucleation and Void Propagation Rate, with Plasmon Excitation (1.1 mW, ~1.50 W/cm<sup>2</sup>, ~1.9 mJ/cm<sup>2</sup> per Pulse) and with No Plasmonic Excitation<sup>a</sup>

conditions	waiting time for void nucleation	void propagation rate
	(s)	$(nm^2/s)$
no plasmonic excitation $(N = 5)$	$2500 \pm 200$	$0.058 \pm 0.008$
plasmonic excitation (N = 4 <sup>b</sup> )	$1490 \pm 90$	$0.109 \pm 0.032$

<sup>&</sup>lt;sup>a</sup>Tabulated values represent average ± standard error across N nanoparticles.

<sup>&</sup>lt;sup>b</sup>One nanoparticle was deemed an outlier on the basis of its markedly different progression of hollowing and was therefore excluded from this statistical analysis. See discussion in the Supporting Information and Fig. S6.

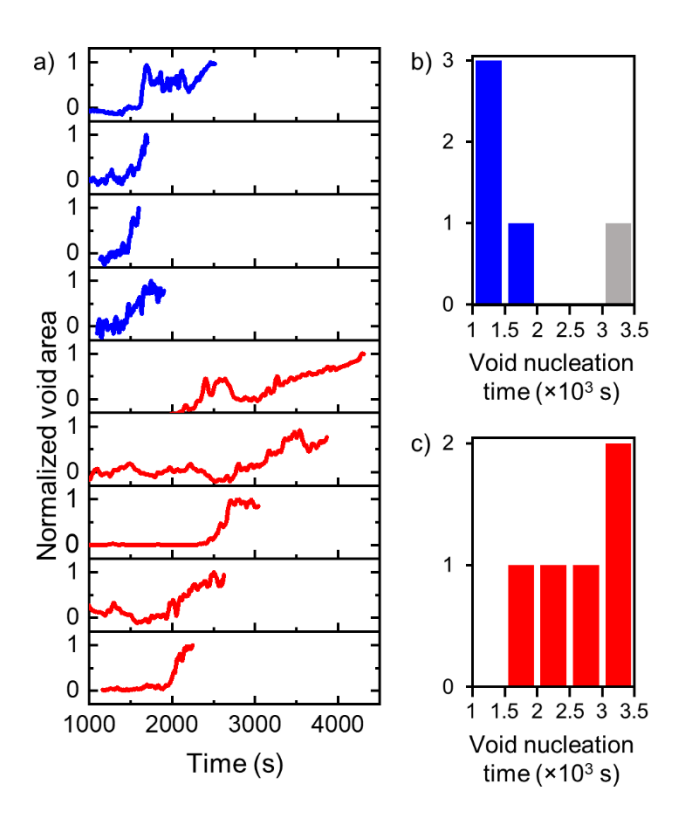


Figure 4 | Kinetics of hollowing with and without plasmon excitation. (a) Time trajectory of the void area (normalized to maximum value) for four individual nanoparticles undergoing hollowing under plasmon excitation (blue curves) and five nanoparticles undergoing hollowing without plasmonic excitation (red curves). The x-axis quantity corresponds to the time in the recorded movie; the start of the movie, i.e., 0 s, was within several (<10) seconds of the onset of electron beam/laser irradiation. The waiting time for a void to nucleate was determined for each case. Histograms of these waiting times for nanoparticles undergoing hollowing (b) under plasmonic excitation and (c) without plasmonic excitation. For one nanoparticle studied under plasmonic excitation (gray bar), the progression of hollowing was atypical, consequently its waiting time was deemed to be an outlier (see discussion in the Supporting Information and Fig. S6). The Supporting Information describes how the time trajectories were generated and waiting times were determined. The waiting times are tabulated in Table S2. For the histograms in panels b and c, a range of 1000–3500 s and a bin of 500 s were used.

Next, we investigated the mechanism of plasmon-enhanced void nucleation. One consequence of plasmonic excitation is the photothermal heating of the nanoparticle by the dissipation of photoexcited carriers via electron-phonon scattering in the Cu core. The photodeposited heat is transported away from the nanoparticle, primarily by conduction through the substrate. Due to the effect of photothermal heating, the temperature of the nanoparticle and the medium around it will be higher under plasmonic excitation than in the absence of plasmonic excitation. To investigate the impact of an elevated temperature, we studied the temperature dependence of the kinetics of hollowing of nanoparticles in the absence of plasmonic excitation for a qualitative comparison with the effect of plasmonic excitation. Using a

microelectromechanical systems (MEMS)-based heating holder, we heated the substrate to steady-state temperatures of 64 °C and 90 °C. We compared the kinetics of hollowing at these conditions with those with no heating by the holder (Table 2 and Table S3). The electron dose rates were maintained to be similar across these experiments performed at different temperatures. The method and parameters are discussed in the "Temperature-dependence study conducted with the heating holder" section in the Supporting Information.

Table 2 | Kinetics of Hollowing, i.e., Waiting Time for Void Nucleation and Void Propagation Rate, at Different Steady-State Temperatures in the Absence of Plasmonic Excitation<sup>a</sup>

Substrate heating condition	Waiting time for void nucleation	Void propagation rate
	<b>(s)</b>	$(nm^2/s)$
No external heating (N =3)	$1100 \pm 600$	$0.07 \pm 0.04$
64 °C (N = 7)	$600 \pm 200$	$0.44 \pm 0.05$
90 °C (N = 3)	$700 \pm 100$	$0.49 \pm 0.07$

<sup>a</sup>Tabulated values represent average  $\pm$  standard error across N trials. Note that one nanoparticle imaged at 90 °C was not included in this analysis because no void nucleation was detected. Furthermore, in hollowing activated by substrate heating, voids preferentially nucleate at the nanoparticle–substrate interface (Figure 5d) interface; therefore, voids may have been detected in the 2D projection well after they were formed. This may have introduced systematic errors in the waiting times.

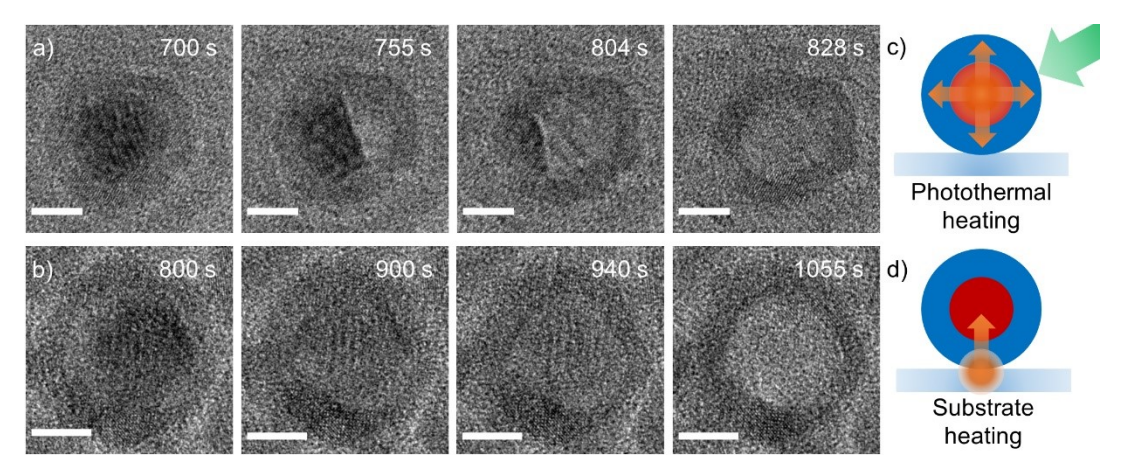


Figure 5 | Comparison of hollowing triggered by plasmonic excitation with that triggered by substrate heating. Selected frames from a movie of the hollowing of (a) a nanoparticle under plasmonic excitation and (b) another that was heated to a steady-state temperature of 90 °C in the absence of plasmonic excitation. Scheme illustrating the progression of heat: (c) under plasmonic excitation, the nanoparticle is heated isotropically from the core, whereas (d) under heating by the holder, the nanoparticle is heated from the bottom via the substrate. Scale bars in the images are 5 nm in length.

The waiting time for nucleation is shorter, on average, at elevated temperatures than at room temperature; however, the large variance in the waiting times prevents us from assigning statistical significance to this trend, as confirmed by a t-test (p > 0.05). The rate of void propagation was significantly higher at elevated temperatures (64 °C and 90 °C) than for the case with no heating by the holder (t-test, p < 0.05); however, the void propagation rates at elevated temperature were similar. Thus, there are qualitative similarities between the effect of an elevated temperature and that of plasmonic excitation on the kinetics of hollowing. Therefore, plasmon-induced heating is a likely source of the enhanced kinetics. However, without knowing the precise temperature of the nanoparticles under irradiation and performing a control experiment in the absence of plasmonic excitation at this temperature, we cannot quantify how much of the kinetic enhancement is due to photothermal heating nor can we fully rule out the contribution of nonthermal effects involving photoexcited carriers or electric fields.

Out of 11 instances of hollowing under substrate heating (64 °C or 90 °C), void nucleation was detected prior to the onset of hollowing in only a minority of instances. In a majority of instances (7 of 11), the image contrast of the core decreased (a sign of hollowing) prior to the visible formation of a void. For instance, in the example presented in Fig. 5b, no void nucleus is detected whereas significant hollowing is evident by 940 s. It is likely that in these cases the void nucleated at a significant depth within the nanoparticle, i.e., near the nanoparticle—substrate interface (Fig. 5d), such that it is not visualized in the 2D projection. Such an occurrence would be consistent with the transfer of heat from the heated substrate to the nanoparticle. Hollowing then occurs by this nucleated void growing in the direction perpendicular to the plane of the substrate and the propagation of the void is not visualized. In plasmon-assisted hollowing (Fig. 5a), a void is instead detected in the 2D projection and is subsequently observed to grow. This is because plasmonic heating is centered within the light-absorbing Cu core (Fig. 5c). Consequently, in plasmon-assisted hollowing, there is no preferred location in the core for the void to nucleate or a preferred direction for the growth of the void.

In summary, using a TEM equipped with optical excitation of the specimen, we studied Cu–Cu<sub>2</sub>O core–shell nanoparticles under simultaneous light excitation and electron-beam irradiation. The nanoparticles underwent hollowing concomitant with the growth of a thin film of Cu<sub>2</sub>O on the substrate around the nanoparticle. Hollowing was induced by electron-beam

irradiation, but kinetically enhanced by plasmonic excitation primarily through the effect of photothermal heating. By monitoring the progress of hollowing with subnanoparticle spatial resolution in real time, we captured the nucleation and propagation of voids within the core. This study establishes the power of optical-excitation-equipped TEM for real-time, atomic-resolution studies of processes in materials under light irradiation.

**Supporting information:** The Supporting Information is available free of charge at https://pubs.acs.org/doi/10.1021/acs.nanolett.3c01474.

Details of methods and analysis, tabulated overview of spatiotemporal behavior of plasmon-assisted nanoparticle hollowing observed in a large set of movies acquired, additional examples of snapshots from movies capturing plasmon-assisted hollowing, thin film characterization, results from control experiment to determine the role of electron-beam irradiation, table of parameters determined from the kinetic analysis of movies of hollowing studied in the presence and absence of plasmonic excitation, results of the outlier nanoparticle in the plasmon-assisted hollowing, tabulated parameters from kinetic analysis of movies of nanoparticles undergoing hollowing in the temperature-dependence study without any plasmonic excitation, and captions for the Supporting Movie 1. Document is available at https://pubs.acs.org/doi/suppl/10.1021/acs.nanolett.3c01474/suppl file/nl3c01474 si 001.pdf.

Supporting Movie 1 of a nanoparticle undergoing hollowing under plasmonic excitation at https://pubs.acs.org/doi/suppl/10.1021/acs.nanolett.3c01474/suppl\_file/nl3c01474\_si\_002.avi.

# **Acknowledgements:**

Funding for this work was provided in part (support for F.M.A) by the Robert C. and Carolyn J. Springborn Endowment and the Future Interdisciplinary Research Explorations (FIRE) grant from the UIUC College of Agricultural, Consumer, and Environmental Sciences. P.K.J. is thankful for the support of the John Simon Memorial Guggenheim Foundation in the form of a Guggenheim Fellowship. R.M.v.d.V was supported by a Packard Fellowship in Science and Engineering from the David and Lucile Packard Foundation. This material is based in part on work supported by the National Science Foundation under Grant No. CHE-1828671. The work was carried out in part at the Materials Research Laboratory Central Research Facilities, University of Illinois. We acknowledge Dr. Jim Mabon and Dr. Changqiang Chen for maintenance of the TEM instrument.

## **Author Contributions**

F.M.A. prepared and characterized materials, designed and conducted experiments, performed analyses, and co-wrote the manuscript. R.M.v.d.V. conceived the project, designed studies, contributed analyses and models, and co-wrote the manuscript. P.K.J. conceived the project, designed studies, provided analyses, models, and interpretation, and co-wrote the manuscript.

#### **References:**

- (1) Brongersma, M. L.; Halas, N. J.; Nordlander, P. Plasmon-Induced Hot Carrier Science and Technology. *Nat. Nanotechnol.* **2015**, *10*, 25–34. https://doi.org/10.1038/nnano.2014.311.
- (2) Wang, L.; Hasanzadeh Kafshgari, M.; Meunier, M. Optical Properties and Applications of Plasmonic-Metal Nanoparticles. *Adv. Funct. Mater.* **2020**, *30*, 2005400. https://doi.org/10.1002/adfm.202005400.
- (3) Linic, S.; Aslam, U.; Boerigter, C.; Morabito, M. Photochemical Transformations on Plasmonic Metal Nanoparticles. *Nat. Mater.* **2015**, *14*, 567–576. https://doi.org/10.1038/nmat4281.
- (4) Yu, S.; Wilson, A. J.; Heo, J.; Jain, P. K. Plasmonic Control of Multi-Electron Transfer and C-C Coupling in Visible-Light-Driven CO<sub>2</sub> Reduction on Au Nanoparticles. *Nano Lett.* **2018**, *18*, 2189–2194. https://doi.org/10.1021/acs.nanolett.7b05410.
- (5) Swearer, D. F.; Zhao, H.; Zhou, L.; Zhang, C.; Robatjazi, H.; Martirez, J. M. P.; Krauter, C. M.; Yazdi, S.; McClain, M. J.; Ringe, E.; Carter, E. A.; Nordlander, P.; Halas, N. J. Heterometallic Antenna-Reactor Complexes for Photocatalysis. *Proc. Natl. Acad. Sci. U. S. A.* **2016**, *113*, 8916–8920. https://doi.org/10.1073/pnas.1609769113.
- (6) Yang, J.; Guo, Y.; Lu, W.; Jiang, R.; Wang, J. Emerging Applications of Plasmons in

- Driving CO<sub>2</sub> Reduction and N<sub>2</sub> Fixation. *Adv. Mater.* **2018**, *30*, 1802227. https://doi.org/10.1002/adma.201802227.
- (7) Kneipp, J.; Kneipp, H.; Kneipp, K. SERS—a Single-Molecule and Nanoscale Tool for Bioanalytics. *Chem. Soc. Rev.* **2008**, *37*, 1052–1060. https://doi.org/10.1039/b708459p.
- (8) Kneipp, K.; Wang, Y.; Kneipp, H.; Perelman, L. T.; Itzkan, I.; Dasari, R. R.; Feld, M. S. Single Molecule Detection Using Surface-Enhanced Raman Scattering (SERS). *Phys. Rev. B Condens. Matter Mater. Phys.* **1997**, *78*, 1667–1670. https://doi.org/10.1103/PhysRevLett.78.1667.
- (9) Devasia, D.; Wilson, A. J.; Heo, J.; Mohan, V.; Jain, P. K. A Rich Catalog of C–C Bonded Species Formed in CO<sub>2</sub> Reduction on a Plasmonic Photocatalyst. *Nat. Commun.* **2021**, *12*, 2612. https://doi.org/10.1038/s41467-021-22868-9.
- (10) Gurav, D. D.; Jia, Y.; Ye, J.; Qian, K. Design of Plasmonic Nanomaterials for Diagnostic Spectrometry. *Nanoscale Adv.* **2019**, *1*, 459–469. https://doi.org/10.1039/c8na00319j.
- (11) Ayala-Orozco, C.; Urban, C.; Knight, M. W.; Urban, A. S.; Neumann, O.; Bishnoi, S. W.; Mukherjee, S.; Goodman, A. M.; Charron, H.; Mitchell, T.; Shea, M.; Roy, R.; Nanda, S.; Schiff, R.; Halas, N. J.; Joshi, A. Au Nanomatryoshkas as Efficient Near-Infrared Photothermal Transducers for Cancer Treatment: Benchmarking against Nanoshells. ACS Nano 2014, 8, 6372–6381. https://doi.org/10.1021/nn501871d.
- (12) Clavero, C. Plasmon-Induced Hot-Electron Generation at Nanoparticle/Metal-Oxide Interfaces for Photovoltaic and Photocatalytic Devices. *Nat. Photonics* **2014**, *8*, 95–103. https://doi.org/10.1038/nphoton.2013.238.
- (13) Oulton, R. F.; Sorger, V. J.; Zentgraf, T.; Ma, R. M.; Gladden, C.; Dai, L.; Bartal, G.; Zhang, X. Plasmon Lasers at Deep Subwavelength Scale. *Nature* **2009**, *461*, 629–632. https://doi.org/10.1038/nature08364.
- (14) Ma, R. M.; Oulton, R. F.; Sorger, V. J.; Zhang, X. Plasmon Lasers: Coherent Light Source at Molecular Scales. *Laser Photonics Rev.* **2013**, *7*, 1–21. https://doi.org/10.1002/lpor.201100040.
- (15) Manjavacas, A.; Liu, J. G.; Kulkarni, V.; Nordlander, P. Plasmon-Induced Hot Carriers in Metallic Nanoparticles. *ACS Nano* **2014**, *8*, 7630–7638. https://doi.org/10.1021/nn502445f.
- (16) Sherry, L. J.; Chang, S.-H.; Schatz, G. C.; van Duyne, R. P. Localized Surface Plasmon Resonance of Single Silver Nanocubes. *Nano Lett.* **2005**, *5*, 2034–2038. https://doi.org/10.4028/www.scientific.net/AMR.818.137.
- (17) Jain, P. K.; Lee, K. S.; El-Sayed, I. H.; El-Sayed, M. A. Calculated Absorption and Scattering Properties of Gold Nanoparticles of Different Size, Shape, and Composition: Applications in Biological Imaging and Biomedicine. *J. Phys. Chem. B* **2006**, *110*, 7238–7248. https://doi.org/10.1021/jp057170o.
- (18) Salmon, A. R.; Kleemann, M. E.; Huang, J.; Deacon, W. M.; Carnegie, C.; Kamp, M.; de Nijs, B.; Demetriadou, A.; Baumberg, J. J. Light-Induced Coalescence of Plasmonic Dimers and Clusters. *ACS Nano* **2020**, *14*, 4982–4987. https://doi.org/10.1021/acsnano.0c01213.
- (19) Ingham, B.; Lim, T. H.; Dotzler, C. J.; Henning, A.; Toney, M. F.; Tilley, R. D. How Nanoparticles Coalesce: An in Situ Study of Au Nanoparticle Aggregation and Grain Growth. *Chem. Mater.* **2011**, *23*, 3312–3317. https://doi.org/10.1021/cm200354d.
- (20) Marimuthu, A.; Zhang, J.; Linic, S. Tuning Selectivity in Propylene Epoxidation by Plasmon Mediated Photo-Switching of Cu Oxidation State. *Science* **2013**, *339*, 1590–1593. https://doi.org/10.1126/science.1231631.
- (21) Rice, K. P.; Paterson, A. S.; Stoykovich, M. P. Nanoscale Kirkendall Effect and Oxidation

- Kinetics in Copper Nanocrystals Characterized by Real-Time, in Situ Optical Spectroscopy. *Part. Part. Syst. Charact.* **2015**, *32*, 373–380. https://doi.org/10.1002/ppsc.201400155.
- (22) Nilsson, S.; Albinsson, D.; Antosiewicz, T. J.; Fritzsche, J.; Langhammer, C. Resolving Single Cu Nanoparticle Oxidation and Kirkendall Void Formation with In Situ Plasmonic Nanospectroscopy and Electrodynamic Simulations. *Nanoscale* **2019**, *11*, 20725–20733. https://doi.org/10.1039/c9nr07681f.
- (23) Susman, M. D.; Feldman, Y.; Bendikov, T. A.; Vaskevich, A.; Rubinstein, I. Real-Time Plasmon Spectroscopy Study of the Solid-State Oxidation and Kirkendall Void Formation in Copper Nanoparticles. *Nanoscale* **2017**, *9*, 12573–12589. https://doi.org/10.1039/c7nr04256f.
- (24) Smith, J. G.; Yang, Q.; Jain, P. K. Identification of a Critical Intermediate in Galvanic Exchange Reactions by Single-Nanoparticle-Resolved Kinetics. *Angew. Chemie Int. Ed.* **2014**, *53*, 2867–2872. https://doi.org/10.1002/anie.201309307.
- (25) Routzahn, A. L.; Jain, P. K. Single-Nanocrystal Reaction Trajectories Reveal Sharp Cooperative Transitions. *Nano Lett.* **2014**, *14*, 987–992. https://doi.org/10.1021/nl4044289.
- (26) Tao, F.; Grass, M. E.; Zhang, Y.; Butcher, D. R.; Renzas, J. R.; Liu, Z.; Chung, J. Y.; Mun, B. S.; Salmeron, M.; Somorjai, G. A. Reaction-Driven Restructuring of Rh-Pd and Pt-Pd Core-Shell Nanoparticles. *Science* **2008**, *322*, 932–934. https://doi.org/10.1126/science.1164170.
- (27) Gibson, E. K.; Beale, A. M.; Catlow, C. R. A.; Chutia, A.; Gianolio, D.; Gould, A.; Kroner, A.; Mohammed, K. M. H.; Perdjon, M.; Rogers, S. M.; Wells, P. P. Restructuring of AuPd Nanoparticles Studied by a Combined XAFS/DRIFTS Approach. *Chem. Mater.* **2015**, *27*, 3714–3720. https://doi.org/10.1021/acs.chemmater.5b00866.
- (28) Tao, F.; Grass, M. E.; Zhang, Y.; Butcher, D. R.; Aksoy, F.; Aloni, S.; Altoe, V.; Alayoglu, S.; Renzas, J. R.; Tsung, C. K.; Zhu, Z.; Liu, Z.; Salmeron, M.; Somorjai, G. A. Evolution of Structure and Chemistry of Bimetallic Nanoparticle Catalysts under Reaction Conditions. *J. Am. Chem. Soc.* **2010**, *132*, 8697–8703. https://doi.org/10.1021/ja101502t.
- (29) Kashin, A. S.; Ananikov, V. P. Monitoring Chemical Reactions in Liquid Media Using Electron Microscopy. *Nat. Rev. Chem.* **2019**, *3*, 625–637. https://doi.org/10.1038/s41570-019-0133-z.
- (30) Xin, H. L.; Alayoglu, S.; Tao, R.; Genc, A.; Wang, C. M.; Kovarik, L.; Stach, E. A.; Wang, L. W.; Salmeron, M.; Somorjai, G. A.; Zheng, H. Revealing the Atomic Restructuring of Pt-Co Nanoparticles. *Nano Lett.* 2014, 14, 3203–3207. https://doi.org/10.1021/nl500553a.
- (31) Vendelbo, S. B.; Elkjær, C. F.; Falsig, H.; Puspitasari, I.; Dona, P.; Mele, L.; Morana, B.; Nelissen, B. J.; van Rijn, R.; Creemer, J. F.; Kooyman, P. J.; Helveg, S. Visualization of Oscillatory Behaviour of Pt Nanoparticles Catalysing CO Oxidation. *Nat. Mater.* **2014**, *13*, 884–890. https://doi.org/10.1038/nmat4033.
- (32) Chee, S. W.; Tan, S. F.; Baraissov, Z.; Bosman, M.; Mirsaidov, U. Direct Observation of the Nanoscale Kirkendall Effect during Galvanic Replacement Reactions. *Nat. Commun.* **2017**, *8*, 1224. https://doi.org/10.1038/s41467-017-01175-2.
- (33) Bettini, J.; Rodrigues, V.; González, J. C.; Ugarte, D. Real-Time Atomic Resolution Study of Metal Nanowires. *Appl. Phys. A Mater. Sci. Process.* **2005**, *81*, 1513–1518. https://doi.org/10.1007/s00339-005-3388-9.
- (34) Oshima, Y.; Mouri, K.; Hirayama, H.; Takayanagi, K. Development of a Miniature STM Holder for Study of Electronic Conductance of Metal Nanowires in UHV-TEM. *Surf. Sci.* **2003**, *531*, 209–216. https://doi.org/10.1016/S0039-6028(03)00568-5.

- (35) Williamson, M. J.; Tromp, R. M.; Vereecken, P. M.; Hull, R.; Ross, F. M. Dynamic Microscopy of Nanoscale Cluster Growth at the Solid-Liquid Interface. *Nat. Mater.* **2003**, 2, 532–536. https://doi.org/10.1038/nmat944.
- (36) Alcorn, F. M.; Jain, P. K.; van der Veen, R. M. Time-Resolved Transmission Electron Microscopy for Nanoscale Chemical Dynamics. *Nat. Rev. Chem.* **2023**, *7*, 256–272. https://doi.org/10.1038/s41570-023-00469-y.
- (37) Yoshida, H.; Kuwauchi, Y.; Jinschek, J. R.; Sun, K.; Tanaka, S.; Kohyama, M.; Shimada, S.; Haruta, M.; Takeda, S. Visualizing Gas Molecules Interacting with Supported Nanoparticulate Catalysts at Reaction Conditions. *Science* **2012**, *335*, 317–319. https://doi.org/10.1126/science.1213194.
- (38) Barnard, A. S.; Young, N. P.; Kirkland, A. I.; Huis, M. A. Van; K, H. X. Nanogold: A Quantitative Phase Map. *ACS Nano* **2009**, *3*, 1431–1436. https://doi.org/10.1021/nn900220k.
- (39) Chmielewski, A.; Meng, J.; Zhu, B.; Gao, Y.; Guesmi, H.; Prunier, H.; Alloyeau, D.; Wang, G.; Louis, C.; Delannoy, L.; Afanasiev, P.; Ricolleau, C.; Nelayah, J. Reshaping Dynamics of Gold Nanoparticles under H<sub>2</sub> and O<sub>2</sub> at Atmospheric Pressure. *ACS Nano* **2019**, *13*, 2024–2033. https://doi.org/10.1021/acsnano.8b08530.
- (40) Smith, J. G.; Chakraborty, I.; Jain, P. K. In Situ Single-Nanoparticle Spectroscopy Study of Bimetallic Nanostructure Formation. *Angew. Chemie Int. Ed.* **2016**, *55*, 9979–9983. https://doi.org/10.1002/anie.201604710.
- (41) Żak, A. M. Light-Induced in Situ Transmission Electron Microscopy-Development, Challenges, and Perspectives. *Nano Lett.* **2022**, *22*, 9219–9226. https://doi.org/10.1021/acs.nanolett.2c03669.
- (42) Swearer, D. F.; Bourgeois, B. B.; Angell, D. K.; Dionne, J. A. Advancing Plasmon-Induced Selectivity in Chemical Transformations with Optically Coupled Transmission Electron Microscopy. *Acc. Chem. Res.* **2021**, *54*, 3632–3642. https://doi.org/10.1021/acs.accounts.1c00309.
- (43) Vadai, M.; Angell, D. K.; Hayee, F.; Sytwu, K.; Dionne, J. A. In-Situ Observation of Plasmon-Controlled Photocatalytic Dehydrogenation of Individual Palladium Nanoparticles. *Nat. Commun.* **2018**, *9*, 4658. https://doi.org/10.1038/s41467-018-07108-x.
- (44) Sytwu, K.; Vadai, M.; Hayee, F.; Angell, D. K.; Dai, A.; Dixon, J.; Dionne, J. A. Driving Energetically Unfavorable Dehydrogenation Dynamics with Plasmonics. *Science* **2021**, *371*, 280–283. https://doi.org/10.1126/science.abd2847.
- (45) Zhang, L.; Miller, B. K.; Crozier, P. A. Atomic Level in Situ Observation of Surface Amorphization in Anatase Nanocrystals during Light Irradiation in Water Vapor. *Nano Lett.* **2013**, *13*, 679–684. https://doi.org/10.1021/nl304333h.
- (46) Zewail, A. H. Four-Dimensional Electron Microscopy. *Science* **2010**, *328*, 187–194. https://doi.org/10.1126/science.1166135.
- (47) McKenna, A. J.; Eliason, J. K.; Flannigan, D. J. Spatiotemporal Evolution of Coherent Elastic Strain Waves in a Single MoS<sub>2</sub> Flake. *Nano Lett.* **2017**, *17*, 3952–3958. https://doi.org/10.1021/acs.nanolett.7b01565.
- (48) Liu, H.; Gage, T. E.; Singh, P.; Jaiswal, A.; Schaller, R. D.; Tang, J.; Park, S. T.; Gray, S. K.; Arslan, I. Visualization of Plasmonic Couplings Using Ultrafast Electron Microscopy. *Nano Lett.* **2021**, *21*, 5842–5849. https://doi.org/10.1021/acs.nanolett.1c01824.
- (49) Barwick, B.; Flannigan, D. J.; Zewail, A. H. Photon-Induced Near-Field Electron Microscopy. *Nature* **2009**, *462*, 902–906. https://doi.org/10.1038/nature08662.

- (50) Campbell, G. H.; McKeown, J. T.; Santala, M. K. Time Resolved Electron Microscopy for in Situ Experiments. *Appl. Phys. Rev.* **2014**, *1*, 041101. https://doi.org/10.1063/1.4900509.
- (51) Zhang, Y.; Flannigan, D. J. Observation of Anisotropic Strain-Wave Dynamics and Few-Layer Dephasing in MoS<sub>2</sub> with Ultrafast Electron Microscopy. *Nano Lett.* **2019**, *19*, 8216–8224. https://doi.org/10.1021/acs.nanolett.9b03596.
- (52) Liu, H.; Kwon, O. H.; Tang, J.; Zewail, A. H. 4D Imaging and Diffraction Dynamics of Single-Particle Phase Transition in Heterogeneous Ensembles. *Nano Lett.* **2014**, *14*, 946–954. https://doi.org/10.1021/nl404354g.
- (53) van der Veen, R. M.; Kwon, O. H.; Tissot, A.; Hauser, A.; Zewail, A. H. Single-Nanoparticle Phase Transitions Visualized by Four-Dimensional Electron Microscopy. *Nat. Chem.* **2013**, *5*, 395–402. https://doi.org/10.1038/nchem.1622.
- (54) Cremons, D. R.; Plemmons, D. A.; Flannigan, D. J. Femtosecond Electron Imaging of Defect-Modulated Phonon Dynamics. *Nat. Commun.* **2016**, *7*, 11230. https://doi.org/10.1038/ncomms11230.
- (55) Zandi, O.; Sykes, A. E.; Cornelius, R. D.; Alcorn, F. M.; Zerbe, B. S.; Duxbury, P. M.; Reed, B. W.; van der Veen, R. M. Transient Lensing from a Photoemitted Electron Gas Imaged by Ultrafast Electron Microscopy. *Nat. Commun.* 2020, 11, 3001. https://doi.org/10.1038/s41467-020-16746-z.
- (56) Huang, Y.; Liu, Z.; Gao, G.; Xiao, G.; Du, A.; Bottle, S.; Sarina, S.; Zhu, H. Stable Copper Nanoparticle Photocatalysts for Selective Epoxidation of Alkenes with Visible Light. ACS Catal. 2017, 7, 4975–4985. https://doi.org/10.1021/acscatal.7b01180.
- Wu, Y. A.; Mcnulty, I.; Liu, C.; Lau, K. C.; Liu, Q.; Paulikas, A. P.; Sun, C.; Cai, Z.; Guest, J. R.; Ren, Y.; Stamenkovic, V.; Curtiss, L. A.; Liu, Y.; Rajh, T. Facet-Dependent Active Sites of Single Cu<sub>2</sub>O Particle Photocatalyst for CO<sub>2</sub> Reduction to Methanol. *Nat. Energy* 2019, 4, 957–968. https://doi.org/10.1038/s41560-019-0490-3.
- (58) Chee, S. W.; Wong, Z. M.; Baraissov, Z.; Tan, S. F.; Tan, T. L.; Mirsaidov, U. Interface-Mediated Kirkendall Effect and Nanoscale Void Migration in Bimetallic Nanoparticles during Interdiffusion. *Nat. Commun.* 2019, 10, 2831. https://doi.org/10.1038/s41467-019-10623-0.
- (59) Niu, K. Y.; Park, J.; Zheng, H.; Alivisatos, A. P. Revealing Bismuth Oxide Hollow Nanoparticle Formation by the Kirkendall Effect. *Nano Lett.* **2013**, *13*, 5715–5719. https://doi.org/10.1021/nl4035362.
- (60) Niu, K.; Frolov, T.; Xin, H. L.; Wang, J.; Asta, M.; Zheng, H. Bubble Nucleation and Migration in a Lead–Iron Hydr(Oxide) Core–Shell Nanoparticle. *Proc. Natl. Acad. Sci. U. S. A.* **2015**, *112*, 12928–12932. https://doi.org/10.1073/pnas.1510342112.
- (61) Yin, Y.; Rioux, R. M.; Erdonmez, C. K.; Hughes, S.; Somorjal, G. A.; Alivisatos, A. P. Formation of Hollow Nanocrystals Through the Nanoscale Kirkendall Effect. *Science* **2004**, 304, 711–714. https://doi.org/10.1126/science.1096566.
- (62) González, E.; Arbiol, J.; Puntes, V. F. Carving at the Nanoscale: Sequential Galvanic Exchange and Kirkendall Growth at Room Temperature. *Science* **2014**, *334*, 1377–1380. https://doi.org/10.1126/science.1212822.
- (63) Wang, W.; Dahl, M.; Yin, Y. Hollow Nanocrystals through the Nanoscale Kirkendall Effect. *Chem. Mater.* **2012**, *25*, 1179–1189. https://doi.org/10.1021/cm3030928.
- (64) Park, J.; Zheng, H.; Jun, Y. W.; Alivisatos, A. P. Hetero-Epitaxial Anion Exchange Yields Single-Crystalline Hollow Nanoparticles. *J. Am. Chem. Soc.* **2009**, *131*, 13943–13945. https://doi.org/10.1021/ja905732q.

- (65) Railsback, J. G.; Johnston-Peck, A. C.; Wang, J.; Tracy, J. B. Size-Dependent Nanoscale Kirkendall Effect during the Oxidation of Nickel Nanoparticles. *ACS Nano* **2010**, *4*, 1913–1920. https://doi.org/10.1021/nn901736y.
- (66) Cabot, A.; Smith, R. K.; Yin, Y.; Zheng, H.; Reinhard, B. M.; Liu, H.; Alivisatos, A. P. Sulfidation of Cadmium at the Nanoscale. *ACS Nano* **2008**, *2*, 1452–1458. https://doi.org/10.1021/nn800270m.
- (67) Yin, M.; Wu, C. K.; Lou, Y.; Burda, C.; Koberstein, J. T.; Zhu, Y.; O'Brien, S. Copper Oxide Nanocrystals. J. Am. Chem. Soc. 2005, 127, 9506–9511. https://doi.org/10.1021/ja050006u.
- (68) Peña-Rodríguez, O.; Pal, U. Effects of Surface Oxidation on the Linear Optical Properties of Cu Nanoparticles. *J. Opt. Soc. Am. B* **2011**, *28*, 2735. https://doi.org/10.1364/josab.28.002735.
- (69) Latham, A. H.; Wilson, M. J.; Schiffer, P.; Williams, M. E. TEM-Induced Structural Evolution in Amorphous Fe Oxide Nanoparticles. *J. Am. Chem. Soc.* **2006**, *128*, 12632–12633. https://doi.org/10.1021/ja064666q.
- (70) Latham, A. H.; Williams, M. E. Transmission Electron Microscope-Induced Structural Evolution in Amorphous Fe, Co, and Ni Oxide Nanoparticles. *Langmuir* **2008**, *24*, 14195–14202. https://doi.org/10.1021/la7035423.
- (71) Feng, W.; Sun, L. D.; Zhang, Y. W.; Yan, C. H. Solid-to-Hollow Single-Particle Manipulation of a Self-Assembled Luminescent NaYF<sub>4</sub>:Yb,Er Nanocrystal Monolayer by Electron-Beam Lithography. *Small* **2009**, *5*, 2057–2060. https://doi.org/10.1002/smll.200900404.
- (72) Herman, D. A. J.; Cheong, S.; Banholzer, M. J.; Tilley, R. D. How Hollow Structures Form from Crystalline Iron–Iron Oxide Core–Shell Nanoparticles in the Electron Beam. *Chem. Commun.* **2013**, *49*, 6203–6205. https://doi.org/10.1039/c3cc43097a.
- (73) Lewis, E. A.; Slater, T. J. A.; Prestat, E.; Macedo, A.; O'Brien, P.; Camargo, P. H. C.; Haigh, S. J. Real-Time Imaging and Elemental Mapping of AgAu Nanoparticle Transformations. *Nanoscale* **2014**, *6*, 13598–13605. https://doi.org/10.1039/c4nr04837g.
- (74) El Mel, A. A.; Bittencourt, C. In Situ Conversion of Nanostructures from Solid to Hollow in Transmission Electron Microscopes Using Electron Beam. *Nanoscale* **2016**, *8*, 10876–10884. https://doi.org/10.1039/c6nr02293f.
- (75) Yang, Y.; Scholz, R.; Berger, A.; Kim, D. S.; Knez, M.; Hesse, D.; Gösele, U.; Zacharias, M. Transmission Electron Microscopy in Situ Fabrication of ZnO/Al<sub>2</sub>O<sub>3</sub> Composite Nanotubes by Electron-Beam-Irradiation- Induced Local Etching of ZnO/Al<sub>2</sub>O<sub>3</sub> Core/Shell Nanowires. *Small* **2008**, *4*, 2112–2117. https://doi.org/10.1002/smll.200800795.
- (76) Liu, B. H.; Teo, H. W.; Mo, Z. H.; Mai, Z. H.; Lam, J.; Xue, J. M.; Zhao, Y. Z.; Tan, P. K. In Situ TEM Study of Electron-Beam Radiation Induced Boron Diffusion and Effects on Phase and Microstructure Evolution in Nanostructured CoFeB/SiO<sub>2</sub> Thin Film. *J. Appl. Phys.* **2017**, *121*, 015111. https://doi.org/10.1063/1.4973579.
- (77) Dienes, G. J.; Damask, A. C. Radiation Enhanced Diffusion in Solids. *J. Appl. Phys.* **1958**, 29, 1713–1721. https://doi.org/10.1063/1.1723032.
- (78) Wang, Z.; Yang, G.; Zhang, Z.; Jin, M.; Yin, Y. Selectivity on Etching: Creation of High-Energy Facets on Copper Nanocrystals for CO<sub>2</sub> Electrochemical Reduction. *ACS Nano* **2016**, *10*, 4559–4564. https://doi.org/10.1021/acsnano.6b00602.